



High-quality multilayer graphene on insulators via metal catalyst alloying in layer exchange with Bayesian optimization

Journal:	<i>CrystEngComm</i>
Manuscript ID	CE-COM-01-2025-000061.R1
Article Type:	Communication
Date Submitted by the Author:	30-Apr-2025
Complete List of Authors:	Ito, Reno; University of Tsukuba Ishiyama, Takamitsu; University of Tsukuba, Institute of Applied Sciences Nozawa, Koki; University of Tsukuba Kikkawa, Jun; National Institute for Materials Science Suemasu, Takeshi; University of Tsukuba, Institute of Applied Physics Toko, Kaoru; University of Tsukuba, Institute of Applied Sciences

COMMUNICATION

High-quality multilayer graphene on insulators via metal catalyst alloying in layer exchange with Bayesian optimization

R. Ito,^{a,c} T. Ishiyama,^{a,c} K. Nozawa,^a J. Kikkawa,^b T. Suemasu,^a and K. Toko ^{*a}

Received 00th January 20xx,

Accepted 00th January 20xx

DOI: 10.1039/x0xx00000x

The use of alloy catalysts in metal-induced layer exchange synthesis, supported by machine learning techniques, has been demonstrated to contribute to the improvement of multilayer graphene quality directly formed on a glass substrate. This advancement facilitates low-temperature synthesis and broadens the potential applications of multilayer graphene in next-generation devices.

The exceptionally high electrical and thermal conductivity, combined with the mechanical robustness of multilayer graphene (MLG), enable its application across various fields.¹ The primary challenge for practical implementation lies in fabricating high-quality MLG uniformly on diverse substrate types.² Since commonly used substrates have limited heat resistance, minimizing the synthesis temperature of MLG is essential. While the transfer method is well-established for producing high-quality graphene,^{3–5} it remains challenging to achieve large-area and uniform MLG formation via this route. Recently, low-temperature synthesis of MLG has been achieved using vapor-phase growth^{6–10} and solid-phase growth,^{11–13} both leveraging the precipitation phenomenon from metal catalysts. Prior studies have demonstrated that metal-induced layer exchange (MILE), originally developed for group IV semiconductors such as Si and Ge,^{14–16} is also effective for MLG formation.^{17–19} Unlike the conventional cooling-based precipitation approach, MILE employs a metal layer as a template for the MLG, allowing uniform deposition over a wide area with precise thickness control.^{20–22} We identified eight metals capable of enabling MLG formation via MILE, and observed that Ni, Co, and Fe, in particular, facilitate low-temperature synthesis.^{23,24} This method, with synthesis temperatures as low as 350 °C, is suitable for flexible devices that utilize heat-resistant plastic substrates.^{25,26} Conversely, the

cooling-based precipitation approach has the advantages of having better MLG quality and lower synthesis temperatures when employing alloy metals.^{27–29} Similar effects have been reported for MILE in group IV semiconductors.³⁰ However, the use of alloy catalysts in MILE for forming MLG, or for other semiconductor materials, has yet to be explored. Additionally, machine learning techniques, such as Bayesian optimization, have recently been applied in materials development.^{30–35} This study focused on Ni, Co, and Fe, known for their effectiveness in low-temperature MLG formation via MILE, to investigate the effect of alloying on MILE growth behavior. Bayesian optimization was used on ternary alloy catalysts, which proved effective in enhancing MLG quality.

Fig. 1(a) provides a schematic illustration of the MILE process. Following metal deposition, an amorphous carbon (a-C) film was continuously deposited in 50 nm layers on a SiO₂ glass substrate at room temperature. All depositions were performed via radio-frequency magnetron (RF) sputtering (Sanyu Electron SVC-700RF, base pressure of 6.0×10^{-4} Pa) under an Ar plasma. The RF power was maintained at 50 W for metal deposition and 100 W for a-C deposition. The deposition rate was 2.2 nm/min for C. Alloy catalyst deposition was achieved by affixing metal sheets onto a sputtering target (Fig. 1(b)). The alloy composition was controlled by varying the surface area of the metal sheets. Since the deposition rate depended on both the type and area of the metal sheet, a variable sputtering time (4–6 min) was used to achieve a metal film thickness of 50 nm. The purity of both C and the metals was 99.9%. The metal composition was determined by energy-dispersive X-ray (EDX) spectrometry using an Oxford AZtec analysis attached to a scanning electron microscopy (SEM) system (Hitachi-High-Tech SU7000; voltage: 15 kV). After deposition, the films were heat-treated at 600 °C for 1 h in a furnace (Koyo Thermo Systems KTF035N1) with an Ar atmosphere. Following heat treatment, the surface metal layer was removed using a dilute nitric acid solution (6%) for 10 min. Upon removing the metal layer, MLG was observed to uniformly cover the substrate surface (Fig. 1(c)).

^a Institute of Applied Physics, University of Tsukuba, 1-1-1 Tennodai, Tsukuba, Ibaraki 305-8573, Japan

^b National Institute for Materials Science, 1-1 Namiki, Tsukuba 305-0044, Japan

^c These authors contributed equally.

The layer exchange behavior of the samples using single-element metal catalysts was investigated after thermal annealing. Fig. 2(a) presents the out-of-plane ϑ - 2ϑ XRD patterns of the samples prior to metal removal. The XRD patterns were obtained for the samples using a diffractometer (Rigaku SmartLab) equipped with a Ge monochromator (wavelength: 1.54 Å) and a Cu-K α radiation source (voltage: 40 kV, current: 30 mA). The incident angle was varied from 20° to 60° in steps of 0.01°. In all samples, a peak corresponding to the C(002) planes of graphite was observed near 27°, indicating the formation of MLG with orientation parallel to the substrate. Additionally, diffraction peaks originating from each catalyst metal were detected. Notably, the Co sample exhibited a strong preferred orientation along the (111) plane, which may be of interest for applications in magnetic thin films. Fig. 2(b)–(d) show the surface SEM images after removal of the metal films. Each sample exhibited surface topographies with different roughness features. Given that, in the principle of MILE, the metal acts as a template for MLG formation, these morphological differences likely reflect variations in the metal layer morphology during the annealing process.^{15,19} Fig. 2(e) displays the EDX spectra obtained from the MLG surfaces after metal removal. For all samples, the residual metal content in the MLG layer was below the detection limit (~1%), confirming the effective removal of the catalyst metal.

Raman spectroscopy (JASCO NRS-5100; spot diameter: 5 μ m; excitation wavelength: 532 nm) was used to investigate the compositional modulation of Ni_{1-x}Co_x, Ni_{1-y}Fe_y, and Co_{1-z}Fe_z binary alloys and their effectiveness in synthesizing MLG via MILE. Fig. 3(a)–(c) presents the Raman spectra collected from the backside of all samples, revealing characteristic peaks near 1350, 1580, and 2700 cm⁻¹, which correspond to the D, G, and G' bands, respectively, of the graphitic structure.³⁶ These observations indicate that layer exchange occurred in all compositional variants, resulting in successful MLG synthesis on SiO₂ substrates. Fig. 3(d)–(f) shows the G/D intensity ratio, an indicator of MLG crystallinity, derived from the Raman spectra in Fig. 3(a)–(c). In each of the binary alloys, the G/D ratios surpassed those obtained using the corresponding single-element metal catalysts, reaching 3.8 for $x = 0.02$, 5.6 for $y = 0.75$, and 4.5 for $z = 0.14$.

The influence of Ni_{1-x-y}Co_xFe_y ternary alloy composition on the G/D ratio was investigated and optimized using machine learning. We executed Bayesian optimization using a Gaussian process regression algorithm in the Python library GPyOpt, with expected improvement as the acquisition function. The parameters used for Bayesian optimization are summarized in Table 1. In the initial stage, five samples with randomly selected Ni_{1-x-y}Co_xFe_y compositions were prepared, and their G/D ratios were evaluated. As depicted in Fig. 4(a), the G/D ratio was particularly high in the region delineated by blue lines ($x = 0.2$ – 0.6 , $y = 0.1$ – 0.5). Bayesian optimization began from the sixth sample (Fig. 4(b)), utilizing the properties of the five randomly selected samples as initial data points. Through this process, the highest G/D ratio of 6.5 was achieved in the eighth sample, surpassing all previously investigated compositions of single and binary alloys. Subsequently, the expected improvement

diminished with an increasing number of samples, converging to nearly zero after the ninth sample. This outcome indicates that the Bayesian optimization process sufficiently explored the parameter space in the mathematical model. The resulting G/D ratio is higher than that of most low-temperature-synthesized MLGs.^{37–41}

To understand the origin of the enhanced crystallinity observed in MLG synthesized with alloy catalysts, we consider several possible effects^{27–29}. Alloying is known to alter key thermodynamic and kinetic parameters that govern graphene formation. One such factor is the surface energy of the metal catalyst, which influences the wetting and dewetting behavior of the metal layer during annealing. A tailored surface energy in the alloy system may lead to more uniform precipitation and ordering of carbon atoms during the layer exchange process. Moreover, the formation of specific alloy phases can locally affect the solubility and diffusivity of carbon in the catalyst layer. For instance, the addition of Fe is known to increase carbon solubility relative to pure Ni or Co,⁴² while also influencing the phase stability of the metallic layer. Such changes can modulate the carbon transport dynamics and promote controlled segregation at the catalyst–substrate interface. Additionally, the presence of multiple metal species in a ternary alloy can moderate the reaction kinetics, reducing excessive nucleation or stacking faults that commonly occur in fast-growth regimes. This may result in more gradual carbon precipitation and facilitate the lateral expansion of graphene domains, thereby enhancing the overall crystallinity. In this context, the Ni_{0.35}Co_{0.44}Fe_{0.21} composition may represent an optimal balance between catalytic activity and growth kinetics. Taken together, these effects suggest that alloying not only modifies the nucleation behavior but also influences the subsequent growth and stacking process of MLG through complex interplays among surface energy, carbon solubility, and phase stability.

The cross-sectional structure of the Ni_{1-x-y}Co_xFe_y sample (with $x = 0.44$ and $y = 0.21$) which exhibited the highest G/D ratio was examined using transmission electron microscopy (TEM). The electron microscope (Themis Z; Thermo Fisher Scientific Inc.), equipped with a dual EDX detector (XFlash® 6-100; Bruker Co.) and spectrometer (Quantum 970, Gatan Inc.), was operated at 80 kV. Cross sections of the samples were prepared using a focused ion beam microscope (Helios Nanolab 600i). The sample surface was coated with a carbon film to protect it during the focused-ion beam process. As seen in the high-angle annular dark-field scanning TEM image in Fig. 5(a) and the corresponding EDX elemental mappings in Fig. 5(b)–(f), a uniform NiCoFe layer is formed on top of MLG. These findings indicate that MLG was directly formed on the SiO₂ substrate through layer exchange, facilitated by the NiCoFe alloy catalyst. The electron diffraction pattern in Fig. 5(g) confirms that the C{002} planes of MLG are oriented parallel to the substrate, consistent with observations for single-element metal catalysts.¹⁹ Furthermore, the electron energy-loss spectra in Fig. 5(h) exhibit pronounced π^* and σ^* peaks characteristic of graphitic structures.⁴³ These sharply defined peaks corroborate the high crystalline quality of the MLG layer.

Conclusions

The effect of alloy catalysts on MLG synthesis via MILE was investigated. The results indicate that the binary and ternary alloys of Ni, Co, and Fe yield a higher G/D ratio than single-element metal catalysts. By employing Bayesian optimization in a machine learning framework, we efficiently identified the optimal composition of the $\text{Ni}_{1-x-y}\text{Co}_x\text{Fe}_y$ ternary alloy catalyst, achieving a G/D ratio as high as 6.5. This enhancement in MLG crystallinity is likely attributable to the altered graphene nucleation density induced by alloying, which highlights the effectiveness of alloy catalysts in MILE. The insights gained from this study not only advance the synthesis of MLG but may also prove beneficial for developing various functional materials, thereby contributing to progress in next-generation electronics research.

Conflicts of interest

There are no conflicts to declare.

Acknowledgements

This work was financially supported by the JSPS KAKENHI (22K18802) and the JST FOREST Program (JPMJFR222J). The experiments were conducted at the International Center for Young Scientists at NIMS and the Nanotechnology Platform at the University of Tsukuba.

Notes and references

- K.S. Novoselov, A.K. Geim, S. V. Morozov, D. Jiang, Y. Zhang, S. V. Dubonos, I. V. Grigorieva, and A.A. Firsov, *Science*, 2004, **306**, 666.
- K. Kang, Y. Matsumoto, X. Li, J. Jiang, X. Xie, K. Kawamoto, M. Kenmoku, J. H. Chu, W. Liu, J. Mao, K. Ueno and K. Banerjee, *Nat. Electron.*, 2018, **1**, 46.
- S. Biswas and L. T. Drzal, *ACS Appl. Mater. Interfaces*, 2010, **2**, 2293.
- A. A. Balandin, *Nat. Mater.*, 2011, **10**, 569.
- R. Murali, Y. Yang, K. Brenner, T. Beck and J. D. Meindl, *Appl. Phys. Lett.*, 2009, **94**, 243114.
- M. H. Rummeli, A. Bachmatiuk, A. Scott, F. Börrnert, J. H. Warner, V. Hoffman, J.-H. Lin, G. Cuniberti and B. Büchner, *ACS Nano*, 2010, **4**, 4206–4210.
- J.-I. Fujita, T. Hiyama, A. Hirukawa, T. Kondo, J. Nakamura, S. Ito, R. Araki, Y. Ito, M. Takeguchi and W. W. Pai, *Sci. Rep.*, 2017, **7**, 12371.
- H.J. Park, B.W. Ahn, T.Y. Kim, J.W. Lee, Y.H. Jung, Y.S. Choi, Y. Il Song, and S.J. Suh, *Thin Solid Films*, 2015, **587**, 8.
- K. Murakami, S. Tanaka, A. Hirukawa, T. Hiyama, T. Kuwajima, E. Kano, M. Takeguchi and J. Fujita, *Appl. Phys. Lett.*, 2015, **106**, 093112.
- Y. Nakajima, H. Murata, N. Saitoh, N. Yoshizawa, T. Suemasu and K. Toko, *ACS Omega*, 2019, **4**, 6677–6680.
- K. Koshida, K. Gumi, Y. Ohno, K. Maehashi, K. Inoue and K. Matsumoto, *Appl. Phys. Express*, 2013, **6**, 105101.
- J. Kwak, J.H. Chu, J.-K. Choi, S.-D. Park, H. Go, S.Y. Kim, K. Park, S.-D. Kim, Y.-W. Kim, E. Yoon, S. Kodambaka, and S.-Y. Kwon, *Nat. Commun.*, 2012, **3**, 645.
- Y. Chen, J. Wang, P. Schützendübe, Z. Wang and E. J. Mittemeijer, *Carbon N. Y.*, 2020, **159**, 37–44.
- Z. Wang, L. Gu, F. Philipp, J.Y. Wang, L.P.H. Jeurgens, and E.J. Mittemeijer, *Adv. Mater.*, 2011, **23**, 854.
- K. Toko and T. Suemasu, *J. Phys. D. Appl. Phys.*, 2020, **53**, 373002.
- K. Toko, S. Maeda, T. Ishiyama, K. Nozawa, M. Murata and T. Suemasu, *Adv. Electron. Mater.*, 2024, **10**, 2400130.
- H. Murata, K. Toko, N. Saitoh, N. Yoshizawa, and T. Suemasu, *Appl. Phys. Lett.*, 2017, **110**, 33108.
- H. Murata, N. Saitoh, N. Yoshizawa, T. Suemasu, and K. Toko, *Appl. Phys. Lett.*, 2017, **111**, 243104.
- K. Toko and H. Murata, *Nanotechnology*, 2021, **32**, 472005.
- H. Murata, Y. Nakajima, N. Saitoh, N. Yoshizawa, T. Suemasu, and K. Toko, *Sci. Rep.*, 2019, **9**, 4068.
- D. Janke, F. Munnik, J. Julin, R. Hübner, J. Grenzer, C. Wüstefeld, S. Gemming, D. Rafaja and M. Krause, *Carbon N. Y.*, 2020, **159**, 656–667.
- T. Suzuki, H. Murata, Y. Kado, T. Ishiyama, N. Saitoh, N. Yoshizawa, T. Suemasu and K. Toko, *ACS Appl. Mater. Interfaces*, 2022, **14**, 54670–54675.
- Y. Nakajima, H. Murata, N. Saitoh, N. Yoshizawa, T. Suemasu and K. Toko, *ACS Appl. Mater. Interfaces*, 2018, **10**, 41664–41669.
- Y. Nakajima, H. Murata, Y. Kado, R. Matsumura, N. Fukata, T. Suemasu, and K. Toko, *Appl. Phys. Express*, 2020, **13**, 025501.
- H. Murata, K. Nozawa, N. Saitoh, N. Yoshizawa, T. Suemasu and K. Toko, *Appl. Phys. Express*, 2020, **13**, 055502.
- H. Murata, Y. Nakajima, Y. Kado, N. Saitoh, N. Yoshizawa, T. Suemasu and K. Toko, *ACS Appl. Energy Mater.*, 2020, **3**, 8410–8414.
- R. S. Weatherup, B. C. Bayer, R. Blume, C. Ducati, C. Baehtz, R. Schlögl, and S. Hofmann, *Nano Letters.*, 2011, **11**, 4154–4160.
- B. Dai, L. Fu, Z. Zou, M. Wang, H. Xu, S. Wang, and Z. Liu, *Nature Communications*, 2011, **2**, 522.
- E. B. Yutomo, F. A. Noor, and T. Winata, *Physical Chemistry Chemical Physics*, 2022, **25**, 708–723.
- T. Ueno, T. D. Rhone, Z. Hou, T. Mizoguchi, and K. Tsuda, *Materials Discovery* 2016, **4**, 18–21.
- S. Miyagawa, K. Gotoh, K. Kutsukake, Y. Kurokawa, and N. Usami, *Appl. Phys. Express* 2021, **14**, 025503.
- K. Osada, K. Kutsukake, J. Yamamoto, S. Yamashita, T. Kadera, Y. Nagai, T. Horikawa, K. Matsui, I. Takeuchi, T. Ujihara, *Mater. Today Commun.* 2020, **25**, 101538.
- Y. K. Wakabayashi, T. Otsuka, Y. Krockenberger, H. Sawada, Y. Taniyasu, H. Yamamoto, *APL Mater* 2019, **7**, 101114.
- I. Ohkubo, Z. Hou, J.N. Lee, T. Aizawa, M. Lippmaa, T. Chikyow, K. Tsuda, T. Mori, *Materials Today Physics* 2021, **16**, 100296.
- T. Ishiyama, K. Nozawa, T. Nishida, T. Suemasu and K. Toko, *NPG Asia Mater.*, 2024, **16**, 17.
- L.M. Malard, M.A. Pimenta, G. Dresselhaus, and M.S. Dresselhaus, *Phys. Rep.*, 2009, **473**, 51.
- S.-J. Byun, H. Lim, G.-Y. Shin, T.-H. Han, S.H. Oh, J.-H. Ahn, H.C. Choi, and T.-W. Lee, *J. Phys. Chem. Lett.*, 2011, **2**, 493.
- K. Gumi, Y. Ohno, K. Maehashi, K. Inoue, and K. Matsumoto, *Jpn. J. Appl. Phys.*, 2012, **51**, 06FD12.
- M. Sato, M. Takahashi, H. Nakano, Y. Takakuwa, M. Nihei, S. Sato, and N. Yokoyama, *Jpn. J. Appl. Phys.*, 2014, **53**, 04EB05.
- M. Kosaka, S. Takano, K. Hasegawa, and S. Noda, *Carbon*, 2015, **82**, 254.
- Q.-Q. Zhuo, Q. Wang, Y.-P. Zhang, D. Zhang, Q.-L. Li, C.-H. Gao, Y.-Q. Sun, L. Ding, Q.-J. Sun, S.-D. Wang, J. Zhong, X.-H. Sun, and S.-T. Lee, *ACS Nano*, 2015, **9**, 594.
- H. Okamoto, *Desk Handbook Phase Diagram for Binary Alloys*, second ed., ASM International, Ohio, 2000.
- P. K. Chu and L. Li, *Mater. Chem. Phys.* 2006, **96**, 253.

COMMUNICATION

Journal Name

COMMUNICATION

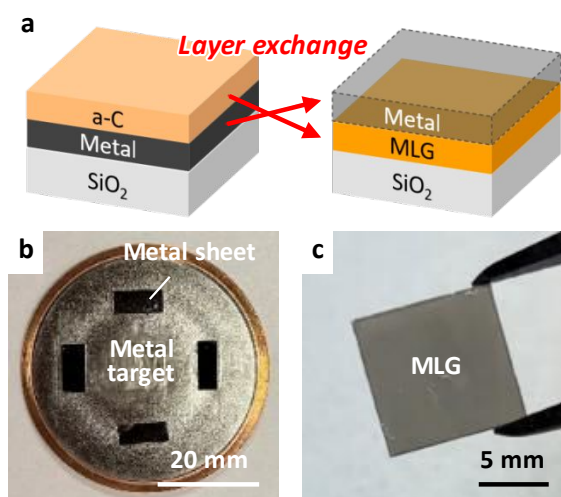


Fig. 1. Fabrication of the samples. (a) Schematic of the sample preparation. Photographs of the (b) sputtering target used for alloy metal deposition and (c) resulting sample after metal removal.

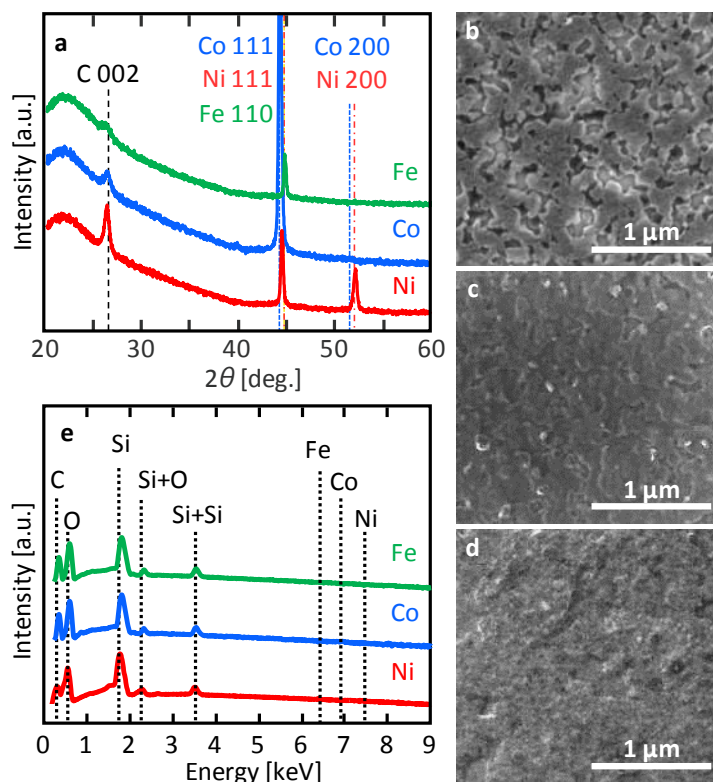


Fig. 2. Characteristics of the samples with single-element metals. (a) θ - 2θ XRD patterns before metal removal. SEM images of the (b) Fe, (c) Co, and (d) Ni samples and (e) EDX spectra after metal removal.

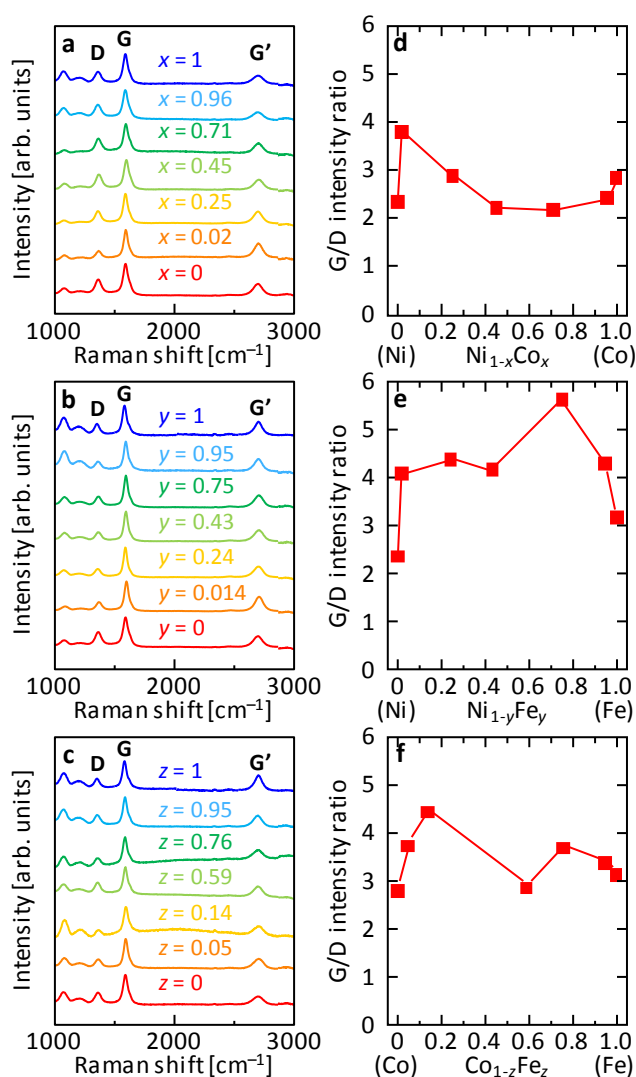


Fig. 3. Effect of binary alloy composition on MLG crystallinity determined from Raman spectroscopy measurements. (a-c) Raman spectra and (d-f) G/D intensity ratio for the (a,d) Ni_{1-x}Co_x, (b,e) Ni_{1-y}Fe_y and (c,f) Co_{1-z}Fe_z samples.

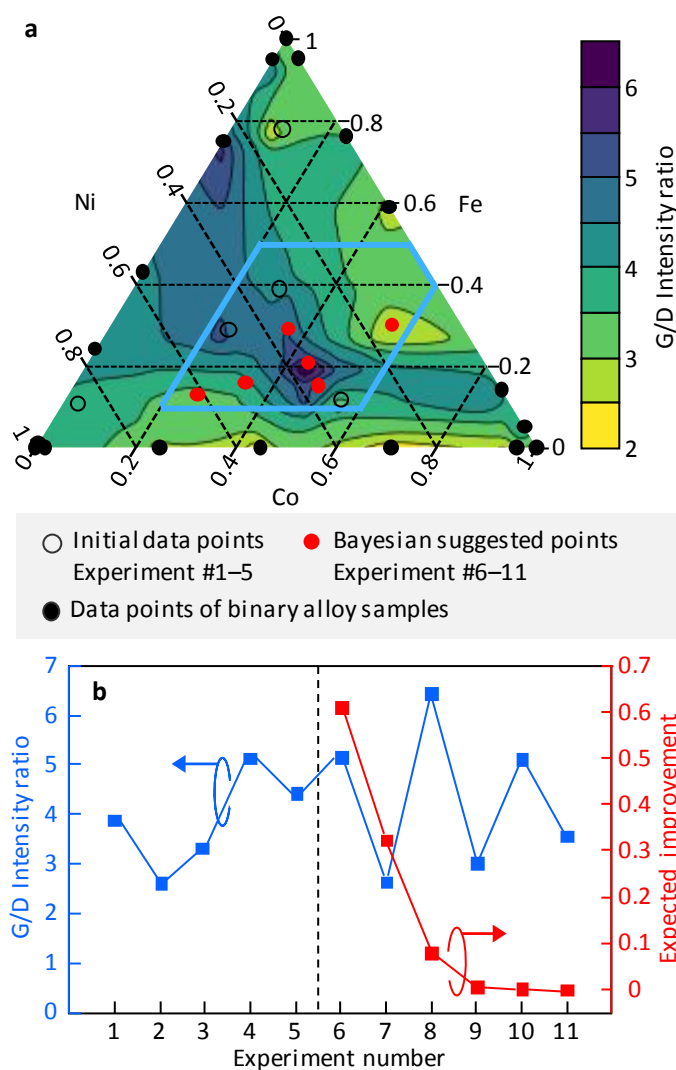


Fig. 4. Bayesian optimization of the composition of $\text{Ni}_{1-x-y}\text{Co}_x\text{Fe}_y$ ternary alloy to improve the G/D intensity ratio. (a) Heatmap showing the relationship between G/D intensity ratio and $\text{Ni}_{1-x-y}\text{Co}_x\text{Fe}_y$ composition, where the area surrounded by the light blue line indicates where Bayesian optimization was performed. (b) G/D intensity ratio and expected improvement of the $\text{Ni}_{1-x-y}\text{Co}_x\text{Fe}_y$ samples with respect to the experiment number.

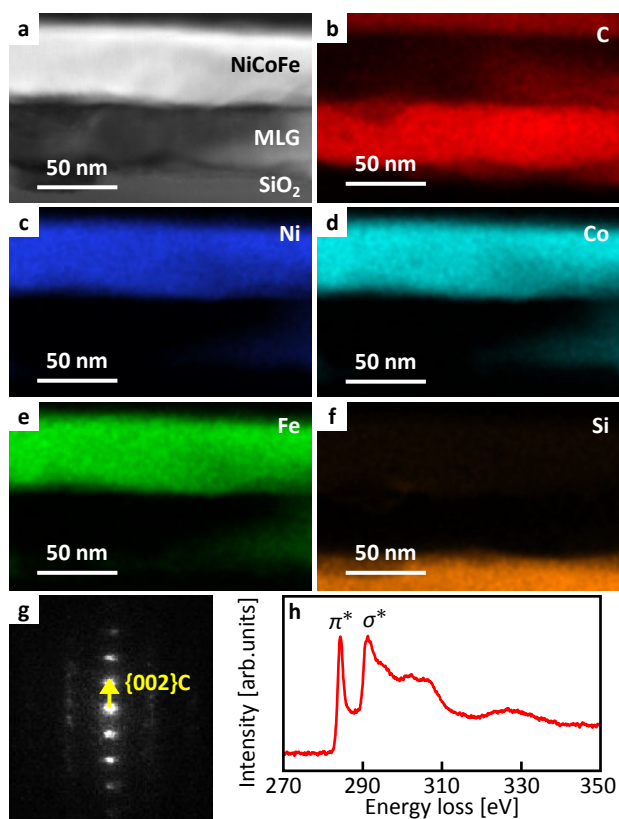


Fig. 5. Characterization of the cross-section of the $\text{Ni}_{0.35}\text{Co}_{0.44}\text{Fe}_{0.21}$ sample. (a) High-angle annular dark-field scanning TEM image. EDX elemental mapping of (b) C, (c) Ni, (d) Co, (e) Fe and (f) Si. (g) Electron diffraction pattern and (h) electron energy-loss spectra of the MLG layer.

Table 1. Summary of the parameters used in Bayesian optimization.

Experiment #	x	y	G/D intensity ratio	Expected improvement
1	0.10	0.78	2.6	
2	0.55	0.12	3.4	
3	0.03	0.19	3.9	
4	0.29	0.39	4.4	
5	0.24	0.29	5.1	
6	0.49	0.15	5.2	
7	0.56	0.30	2.6	0.61033
8	0.44	0.21	6.5	0.32329
9	0.26	0.13	3.0	0.00652
10	0.36	0.29	5.1	0.00138
11	0.34	0.16	3.6	0.00071

Data availability statement

Data for this article are available at Open Science Framework at <https://osf.io/rjkm5>.